Temporal Quantum Fluctuations in the Fringe-Visibility of Atom Interferometers with Interacting Bose-Einstein Condensate

Doron Cohen and Amichay Vardi

Abstract We formulate a semiclassical approach to study the dynamics of coherence loss and revival in a Bose-Josephson dimer. The phase-space structure of the bi-modal system in the Rabi, Josephson, and Fock interaction regimes, is reviewed and the prescription for its WKB quantization is specified. The local density of states (LDOS) is then deduced for any given preparation from its semiclassical projection onto the WKB eigenstates. The LDOS and the non-linear variation of its level-spacing are employed to construct the time evolution of the initial preparation and study the temporal fluctuations of interferometric fringe visibility. The qualitative behavior and characteristic timescales of these fluctuations are set by the pertinent participation number, quantifying the spectral content of the preparation. We employ this methodology to study the Josephson-regime coherence dynamics of several initial state preparations, including a Twin-Fock state and three different coherent states that we denote as 'Zero', 'Pi', and 'Edge' (the latter two are both on-separatrix preparations, while the Zero is the standard ground sate preparation). We find a remarkable agreement between the semiclassical predictions and numerical simulations of the full quantum dynamics. Consequently, a characteristic distinct behavior is implied for each of the different preparations.

D. Cohen
Departments of Physics, Ben-Gurion University of the Negev,
P.O. Box 653 84105 Beer-Sheva, Israel

A. Vardi (✉)
Departments of Chemistry, Ben-Gurion University of the Negev,
P.O. Box 653 84105 Beer-Sheva, Israel
e-mail: avardi@bgu.ac.il

Progress Optical Sci., Photonics (2013): 457–472
DOI: 10.1007/10091_2012_2

Published Online: 18 February 2012

1 Introduction

Atom interferometry [1–4] with Bose-condensed atoms offers the possibility of constructing compact and highly precise measurement tools. Recent experiments [5–20] demonstrate that bi-modal Bose-Einstein condensates (BECs) have the necessary phase-coherence and controllability of coupling and interaction parameters, to operate atom interferometers at the best sensitivity allowed by quantum mechanics.

A typical atom interferometer follows the Mach-Zehnder scheme consisting of a preparation stage, in which the bimodal input state is mixed by a (usually 50:50) beam-splitter, a waiting time t during which the system evolves and the two modes acquire a relative phase difference φ, and a measurement stage where the two condensates are either released and allowed to interfere or are mixed again by a second beamsplitter. In the former case, the accumulated relative phase φ correlates with the location of interference fringes, whereas in the latter it is reflected in the final atom number difference.

The single-particle coherence of the split BEC is characterized by the many-realizations fringe-visibility function $g_{12}^{(1)}(t)$. The useful timescale of an interferometric measurement is set by decoherence. For trapped BEC interferometers, an important source for the loss of single-particle coherence, is the phase-diffusion induced by nonlinear inter-particle interactions [9, 21–29]. For uncoupled condensates starting from a coherent preparation, this process amounts to a simple Gaussian decay of $g_{12}^{(1)}(t)$ on a time scale $t \sim (U\sqrt{N})^{-1}$, where U is the interaction strength and N is the number of particles. However, most current atom-interferometer setups with trapped BECs operate in the Josephson interaction regime, where coupling while small, still affects the dynamics and generates richer coherence evolution which includes oscillations, fluctuations, and recurrences of $g_{12}^{(1)}(t)$ due to quantum collapse and revival [30–32]. The evolution of fringe visibility in the Josephson regime, thus offers a unique opportunity for the controlled study of strong correlation dynamics, beyond the usual focus on ground state properties.

Our objective here is to characterize the quantum dynamics of single-particle coherence and explore the dependence of its fluctuations on the initial preparation [32–35]. For this purpose we employ a semiclassical picture of the quantum two-mode Bose-Hubbard model normally used to describe BEC atom interferometers. In Sect. 2 We introduce the model Hamiltonian for N bosons in a dimer system. In Sect. 3 we provide the prescription for the WKB quantization of the associated spherical phase space. Several experimentally viable preparations are introduced in Sect. 4, and their local density of states (LDOS) is characterized using a participation number M, with marked differences in the dependence of M on the particle number N, and on the interaction U. Consequently we are able to analyze the observed temporal fluctuations in Sect. 5 and determine their long time average and their characteristic variance. We show that the RMS of the fluctuations scales differently with N, depending on the nature of the prepared state.

2 Model Hamiltonian and Phase-Space Structure

Matter-wave interferometers can be realized using double-well spatial confinement [5–14] or internal spin states [15–19]. In both cases, the bimodal system of interacting atoms is described to good accuracy [36] by the tight-binding Bose-Hubbard Hamiltonian (BHH) [27–29, 37–39]. Here we refer to N particles in a two-site (bi-modal) system, also known as a 'dimer':

$$\mathcal{H} = \sum_{i=1,2}\left[\mathcal{E}_i\hat{n}_i + \frac{U}{2}\hat{n}_i(\hat{n}_i - 1)\right] - \frac{K}{2}(\hat{a}_2^\dagger\hat{a}_1 + \hat{a}_1^\dagger\hat{a}_2), \tag{1}$$

where K is the hopping amplitude, U is the interaction, and $\mathcal{E}_i$ are the on-site energies. One may define an SU(2) algebra, where

$$J_z \equiv \frac{1}{2}(\boldsymbol{n}_1 - \boldsymbol{n}_2) \equiv \boldsymbol{n}, \tag{2}$$

$$J_+ \equiv \hat{a}_1^\dagger\hat{a}_2, \tag{3}$$

and $J_- = [J_+]^\dagger$. Hence $J_x = (J_+ + J_-)/2$ and $J_y = (J_+ - J_-)/2i$. Rewriting the Hamiltonian (1) in terms of these SU (2) generators, we see it is formally the same as that of a spin $j = N/2$ system,

$$\mathcal{H} = -\mathcal{E}\hat{J}_z + U\hat{J}_z^2 - K\hat{J}_x + \text{const}, \tag{4}$$

where $\mathcal{E} = \mathcal{E}_2 - \mathcal{E}_1$ is the bias in the on-site potentials. It is thus clear that the characteristic dimensionless parameters which determine both stationary and dynamic properties, are

$$u \equiv NU/K \tag{5}$$

$$\varepsilon \equiv \mathcal{E}/K \tag{6}$$

The two-site BHH can be regarded as the quantized version of the top Hamiltonian, whose *spherical* phase space is described by the conjugate non-canonical coordinates $(\boldsymbol{\theta}, \boldsymbol{\varphi})$ that are defined through

$$\hat{J}_z = [(j{+}1)j]^{1/2}\cos(\boldsymbol{\theta}), \tag{7}$$

$$\hat{J}_x = [(j{+}1)j]^{1/2}\sin(\boldsymbol{\theta})\cos(\boldsymbol{\varphi}), \tag{8}$$

The Hamiltonian (4) is thus transformed into the top Hamiltonian,

$$\mathcal{H}(\boldsymbol{\theta}, \boldsymbol{\varphi}) = \frac{NK}{2}\left[\frac{1}{2}u(\cos\boldsymbol{\theta})^2 - \varepsilon\cos\boldsymbol{\theta} - \sin\boldsymbol{\theta}\cos\boldsymbol{\varphi}\right]. \tag{9}$$

which is closely related to the Josephson Hamiltonian. The *cylindrical* phase space of the latter is described by the canonical coordinate $\boldsymbol{n}$ of (2), and its conjugate

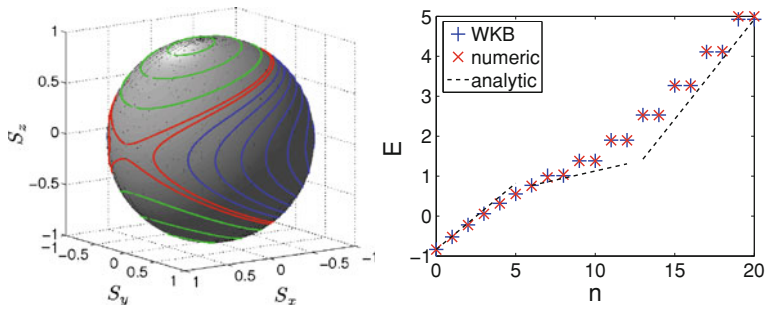

Fig. 1 Contour lines for $u > 2$. Sea levels are colored *blue*, Island levels are colored *green*, and the Separatrix is colored *red* (*left panel*). Energy spectrum for $N = 20$ and $u = 10$. WKB energies (*red x*) are compared with exact eigenvalues (*blue +*). *Dashed lines* indicate slopes ω_J for low energies, ω_x for near-separatrix energies, and ω_+ for high energies (*right panel*)

angle $\boldsymbol{\varphi}$. In the absence of bias, in the vicinity of the Equator, it is just the pendulum Hamiltonian:

$$\mathcal{H}(\boldsymbol{n}, \boldsymbol{\varphi}) \approx U\boldsymbol{n}^2 - \frac{1}{2}KN\cos\boldsymbol{\varphi}\,. \tag{10}$$

In Fig. 1 we draw the constant energy contours $\mathcal{H}(\theta, \varphi) = \text{const}$ of the top Hamiltonian (9) for $u = 10$ and $\varepsilon = 0$. Generally, the qualitative features of the phase-space structure [23, 40], change drastically with the interaction strength. For $u > 1$ a separatrix appears provided $|\varepsilon| < \varepsilon_c$, where

$$\varepsilon_c = \left(u^{2/3} - 1\right)^{3/2}. \tag{11}$$

This separatrix divides the spherical phase space into "sea" and two "islands" as shown in Fig. 1. In what follows, we focus on the case of zero bias. Accordingly we distinguish between three regimes depending on the strength of the interaction [41]:

$$\text{Rabi regime}: \quad u < 1, \tag{12}$$

$$\text{Josephson regime}: 1 < u < N^2, \tag{13}$$

$$\text{Fock regime}: u > N^2. \tag{14}$$

In the Rabi regime the separatrix disappears and the entire phase-space consists of the nearly linear "sea". By contrast, in the Fock regimes the "sea" has area less than $1/N$, and therefore it cannot accommodate quantum states. Thus in the Fock regime phase space is composed entirely of two nonlinear components: the "islands" occupy the entire upper and lower hemispheres. Our main interest below is in the intermediate Josephson regime where linear and non-linear regions coexist and the dynamics is least trivial. This is the regime of interest to most current BEC interferometers and luckily, precisely where semiclassical methods are expected to be most effective.

3 WKB Quantization and Associated Frequencies

Due to the simplicity of the two mode BHH (9), it is possible to carry out its semiclassical quantization analytically [32–34, 42–46] and acquire great insight on the ensuing dynamics of the corresponding Wigner distribution [47, 50]. We begin by accurately determining the quantum energy levels in the Josephson regime, using the WKB prescription. Having a phase-space area of 4π spherical angle supporting $N+1$ quantum states, the Planck cell area is,

$$h = \text{Planck cell area in steradians} = \frac{4\pi}{N+1}, \tag{15}$$

and the WKB quantization condition thus reads,

$$A(E_v) = \left(\frac{1}{2} + v\right)h, \quad v = 0, 1, 2, 3, ..., \tag{16}$$

where $A(E)$ is the phase space area which is enclosed by the energy contour. Note that it does not matter which area, of which "side" of the contour, is selected. Away from the separatrix the levels spacing equals approximately to the classical oscillation frequency:

$$\omega(E) \equiv \frac{dE}{dv} = \left[\frac{1}{h}A'(E)\right]^{-1} \tag{17}$$

In particular in the absence of interaction this is the Rabi frequency

$$\omega_K \approx K \tag{18}$$

For strong interaction, in the bottom of the sea, it is the Josephson frequency

$$\omega_J \approx \sqrt{NUK} = \sqrt{u}\,\omega_K \tag{19}$$

while in the top of the islands it is

$$\omega_+ \approx NU = u\,\omega_K \tag{20}$$

Finally, in the vicinity of the separatrix a more careful analysis is required, leading to the h dependent result

$$\omega_x \approx \left[\log\left(\frac{N^2}{u}\right)\right]^{-1} \omega_J \tag{21}$$

Comparing Eq. (21) to Eqs. (19) and (20) we realize that only in the vicinity of the separatrix does the number of particles N become an essential parameter in the spectral analysis of the dynamics at fixed u.

4 The Preparations

Current experiments in matter-wave interferometry enable the preparation of nearly coherent states of the $SU(2)$ algebra, by fast splitting of the condensate [12]. Alternatively, number-squeezed states, approaching relative-number Fock states for large separation, can be prepared by slow, adiabatic splitting [14]. So far, the main focus of study in the Josephson regime, has been on coherent population dynamics, contrasting coherent preparations located near the bottom of the linear sea which exhibit Josephson oscillations around the ground state [8, 51–54] , with coherent preparations located near the top of the nonlinear islands, which result in self-trapped phase-oscillations around the 'poles' [8, 55]. Our focus here, is on the interesting effects incurred in the *fringe-visibility dynamics* of coherent preparations located *on the separatrix* and contrasting them with the more common ground-state, north-pole, and number-squeezed preparations.

4.1 Wigner Distributions

In order to gain semiclassical insight, it is convenient to represent each eigenstates $|E_v\rangle$ by a proper spin Wigner function [47, 50], which is a quasi-distribution that dwells on the spherical phase space. In this representation these eigenstates corresponds to strips along the contour lines of $\mathcal{H}$. In the same representation Coherent states $|\theta\varphi\rangle$ are like a minimal Gaussian wavepackets, while Fock states $|n\rangle$ are like equi-latitude annulus. Note that the coherent state $\theta = 0$ is also a Fock state with all the particles occupying one site, while $|n = 0\rangle$ is the Twin Fock state with equal number of particles in both sites.

In Fig. 2 we plot the Wigner functions corresponding to the five preparations under study. These include the NorthPole self-trapped state, the TwinFock state, two equal-population coherent states that we call Zero ($\varphi = 0$) and Pi ($\varphi = \pi$,) and a third coherent state preparation that we call Edge. The two latter states (Pi and Edge) are both on-separatrix preparations. Note that in the Zero state all the particles occupy the symmetric orbital, while in the highly excited Pi state all the particles occupy the antisymmetric orbital.

Some of these preparations were experimentally realized and studied [8]. While in the experimental work the emphasis was on contrasting Josephson-Oscillation and Self-Trapping, with regard to near-Zero and near-NorthPole preparations, here our main interest is in contrasting the Zero preparation with the on-separatrix preparations Pi and Edge.

4.2 Local Density of States

In order to analyze the dynamics ensuing from the said preparations, we expand the initial state as a superposition of the eigenstates $|E_v\rangle$. The probability of the vth

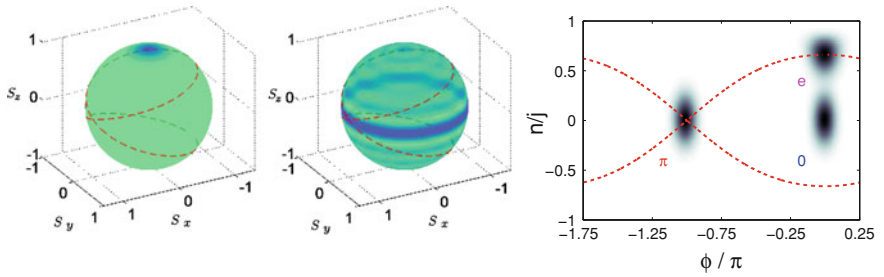

Fig. 2 An illustration of the NorthPole ($\theta = 0$) coherent state preparation (*left*), the TwinFock ($n = 0$) preparation (*middle*), and of Pi ("π"), Zero ("0") and Edge ("e") preparations (*right*) using Wigner plots on a sphere. The *left* and *middle* panels are a 3D plots, while the *right panel* is a Mercator projection of the sphere using $(\boldsymbol{\varphi}, \boldsymbol{n})$ coordinates

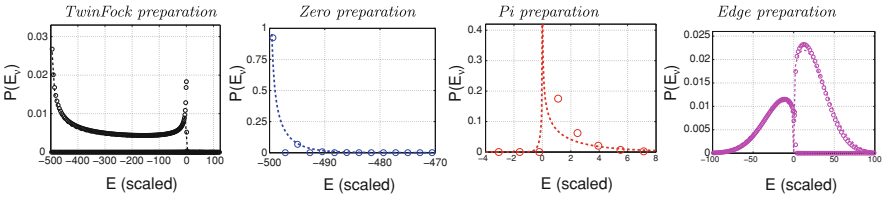

Fig. 3 The LDOS of $N = 500$ bosons with $u = 4$, for TwinFock, Zero, Pi, and Edge preparations (*left* to *right*). The horizontal axes are $E - E_x$ and ω/ω_J. The *lines* in the LDOS figures are based on a semiclassical analysis, while the *circles* are from the exact quantum calculation. Note the outstanding difference between the spectral support of Zero and Pi preparations compared with continuous-like support in the case of Edge and Fock preparations

eigenstate in the superposition is denoted $P(E_v)$, and is known as the local density of states (LDOS) with respect to the pertinent preparation. The LDOS of the various preparations is illustrated in Fig. 3 and the line shape can be determined analytically via a semiclassical calculation [32, 35]. Schematically the results can be summarized as follows:

$$P(E)\Big|_{\text{TwinFock}} \sim \left[1 - \left(\frac{2E}{NK}\right)^2\right]^{-1/2} \tag{22}$$

$$P(E)\Big|_{\text{Zero}} \sim \mathbf{I}\left[\frac{E - E_-}{NU}\right] \tag{23}$$

$$P(E)\Big|_{\text{Pi}} \sim \mathbf{K}\left[\frac{E - E_x}{NU}\right] \tag{24}$$

$$P(E)\Big|_{\text{Edge}} \sim \exp\left[-\frac{1}{N}\left(\frac{E - E_x}{\omega_J}\right)^2\right] \tag{25}$$

where **I** and **K** are Bessel functions. It is important to observe that the classical energy scales are NK and N^2U. Accordingly only the line shape of the TwinFock LDOS has a purely classical interpretation. In contrast to that, the width of the coherent preparations is determined by the quantum uncertainty.

4.3 Participation Number

The qualitative features of the fringe-visibility dynamics, given some initial preparation, are determined by its *participation number* defined as:

$$M \equiv \left[\sum_v P(E_v)^2\right]^{-1} = \text{number of participating levels in the LDOS} \tag{26}$$

In the case of a TwinFock preparation, the Wigner function is spread all over the equator of the spherical phase-space and thus overlaps with all the states in the sea up to the separatrix level (the equator intersects with all sea trajectories in Fig. 2 but with no island trajectory). Therefore we expect M to be of order N, with classical (N independent) prefactor that reflects the relative size of the sea:

$$M = \text{ClassicalPrefactor} \times N, \quad [\text{TwinFock preparation}] \tag{27}$$

In the case of a coherent preparation, the Wigner function is a minimal wavepacket that has width $\sigma_n = (N/2)^{1/2}$. If the Fock states $|n\rangle$ were the eigenstates of the Hamiltonian, as they are in the Fock regime, we would get

$$M = (2\pi N)^{1/2}, \quad [\text{Coherent preparation, } n \text{ basis}], \tag{28}$$

for all three coherent preparations. However in the Josephson regime the eigenstates are $|E_v\rangle$, and therefore the differences between the LDOS of the three coherent states Zero, Pi, and Edge, are set by the ratio between σ_n and the width of the separatrix ($\Delta n = NK/U$). The ratio $\sigma_n/\Delta n$ equals the dimensionless semiclassical parameter $(u/N)^{1/2}$. If this ratio is larger than unity the distinction between the Zero, the Pi and the Edge preparations is blurred, and we expect to have the same participation number. Indeed plotting the participation number of these three initial states (Fig. 4), we see that at the strong interaction limit $M \approx (3/2)N^{1/2}$. This is roughly half compared with Eq. (28), and reflects the odd-even selection rule that removes half of the overlaps (the semiclassical states do not have a well-defined parity with respect to site substitution, whereas the actual quantum eigenstates are constructed from their odd and even superpositions. The participating constituents are those that have the same parity as that of the preparation).

For weaker interaction, when the semiclassical parameter $(u/N)^{1/2}$ is smaller than unity the different nature of the Zero, the Pi and the Edge preparations expresses itself. Now we have to account for both the width of LDOS line shape and the mean level spacing. This leads to the following results:

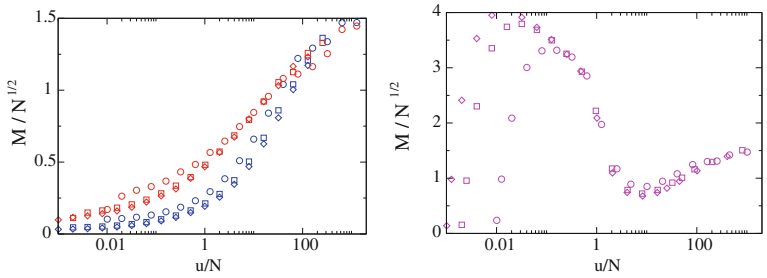

Fig. 4 The participation number M as determined from the LDOS for $N = 100$(*Circle*), 500(*Square*), and 1000(*Diamond*) particles. The *left panel* contains the Zero (*lower set* in *blue*) and Pi (*upper set* in *red*) preparations, while the Edge preparation is presented in the *right panel*. Note the different vertical scale. In the crudest approximation we expect in the Edge case $M \sim N^{1/2}$, while in the Pi case $M \ll N^{1/2}$ as long as $(u/N) \ll 1$

$$M \approx \sqrt{u}, \quad \text{[Zero preparation]} \tag{29}$$

$$M \approx \left[\log\left(\frac{N}{u}\right)\right]\sqrt{u}, \quad \text{[Pi preparation]} \tag{30}$$

$$M \approx \left[\log\left(\frac{N}{u}\right)\right]\sqrt{N}, \quad \text{[Edge preparation]} \tag{31}$$

The striking point here is that the Pi preparation resembles the Zero preparation, rather than its sister separatrix Edge state. This seems at first sight in contradiction with semiclassical intuition: one would naively expect that wavepackets that have the same energy and reside in the same phase space region (separatrix) would behave similarly. This is not the case, as we see here, and later in the dynamical analysis. The Pi state is actually closer to the Zero preparation, as both have a small participation value. The resemblance of the Pi and Edge preparations is only detectable in the formal limit $N \to \infty$. In other words, because of the N dependence of M it is "easier" to approach the "classical limit" in the case of an Edge preparation.

5 Coherence Dynamics

5.1 Classical, Semiclassical, and Quantum Dynamics of the Bloch Vector

In this section, we describe the dynamics of single-particle coherence for the preparations of Sect. 4. The lowest-order approximation is the *mean field* dynamics. It is generated by replacing the operators in the Hamiltonians of

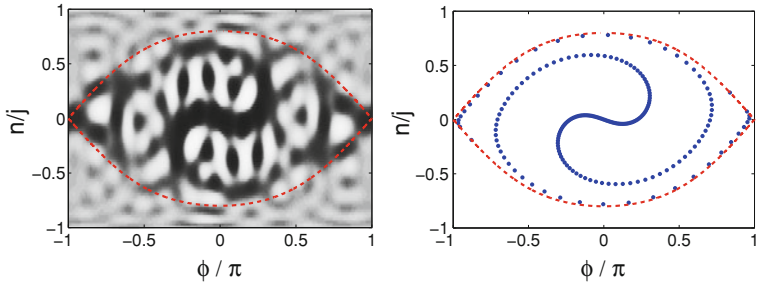

Fig. 5 The evolving quantum state of $N = 40$ bosons with $u = 5$ for TwinFock ($n = 0$) preparation. The units are such that $K = 1$ and the time is $t = 4$. On the *left*—the Wigner function of the evolved quantum state. On the *right*— the corresponding classical evolution

Eqs. (1), (4), or (9) by c-numbers, thus obtaining a set of classical equations of motion for them. For example, in the spin representation,

$$\begin{aligned} \dot{J}_x &= (\mathcal{E} - 2UJ_z)J_y, \\ \dot{J}_y &= KJz - (\mathcal{E} - 2UJ_z)J_x, \\ \dot{J}_z &= -KJ_y. \end{aligned} \tag{32}$$

These Gross-Pitaevskii equations (GPE) describe the *classical* evolution of a *point* in phase space, which is a single trajectory. The classical evolution assumes that the state of the system is coherent at all times, so that the single-particle coherence is fixed to unity and the Wigner distribution always resembles a minimal Gaussian (the center of which is the traced point). By contrast, the *semi-classical* theory describes the classical evolution and subsequent deformation of a *distribution* in phase space, according to the GPE equations (34). Finally the *Quantum theory* is obtained by direct solution of the Schrödinger or Heisenberg equations with the Hamiltonians (1), (4), or (9). This full quantum solution adds recurrences and fluctuations which are absent from the classical and semiclassical pictures and result from the discreteness of the energy spectrum. The dimer system is integrable, and therefore the WKB method provides a very good basis for the analysis. Fig. 5 illustrates the agreement between the quantum evolution of the Wigner function, starting from the TwinFock state [33, 35] and the semiclassical evolution of a corresponding distribution. It should be emphasized that in the Wigner-Wyle formalism any operator $\hat{A}$ is presented by the phase-space function $A_W(\Omega)$, and the calculation of an expectation value can be done in a classical-like formulation:

$$\langle \hat{A} \rangle = \mathrm{trace}[\hat{\rho}\hat{A}] = \int \frac{d\Omega}{h} \rho_W(\Omega) A_W(\Omega)\,. \tag{33}$$

The single-particle density matrix of the two-mode system can be presented using the Bloch vector,

$$\vec{\boldsymbol{S}} = \langle \vec{\boldsymbol{J}} \rangle / (N/2) = (S_x, S_y, S_z), \tag{34}$$

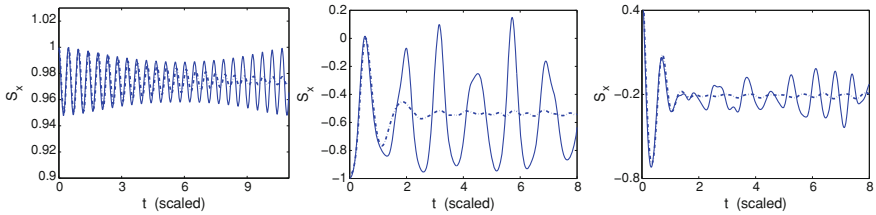

Fig. 6 The variation of $S_x(t)$ with time for $N = 40$ particles with $u = 5$, for Zero (*left*), Pi (*middle*), and Edge (*right*) preparations. Note the different vertical scale. The *dashed-dotted* lines are based on semiclassical simulation

Whereas previous work [8] has focused on the mean-field dynamics of the occupation difference $(N/2)\langle S_z\rangle$, here we study the *single-particle coherence* manifested in the one body purity,

$$\text{OneBodyPurity} = (1/2)\left[1 + \langle S_x\rangle^2 + \langle S_y\rangle^2 + \langle S_z\rangle^2\right], \tag{35}$$

and the transverse component of the Bloch vector, the fringe visibility,

$$g_{12}^{(1)} = \left[\langle S_x\rangle^2 + \langle S_y\rangle^2\right]^{1/2}. \tag{36}$$

This quantity reflects the fringe-contrast over multiple runs of an experiment in which the particles from the two confined modes are released and allowed to interfere. In Fig. 6 we plot examples for the evolution of the Bloch vector, and observe significant differences in the dynamical behavior of the Zero, Pi, and Edge preparations. Our objective is to understand how the dynamics depends on the dimensional parameters: the "classical" parameter u and the "quantum" parameter N.

In accordance with the opening paragraph of this section, we see in Fig. 6 that in the semiclassical simulation the fluctuations always die after a transient. This should be contrasted with both the *classical* (single trajectory) behavior, and the *quantum* behavior. In the latter quantum case the wavepacket is a superposition of $M > 1$ eigenstates, and consequently there are persistent fluctuations that depend on the "quantum" parameter N. In what follows, we will quantitatively analyze the characteristic features of the quantum dynamics resulting from the three coherent preparations, including the frequency of oscillation, its mean long-time value, and its RMS amplitude, and compare the analytic predictions to the numerical results at various values of the characteristic parameter u/N.

5.2 Characteristic Frequencies

The typical frequency of the fluctuations is the simplest characteristic that differentiate the three panels of Fig. 6. The numerically-obtained frequency ω_{osc} as a function of the interaction parameter u/N is displayed in Fig. 7. In the

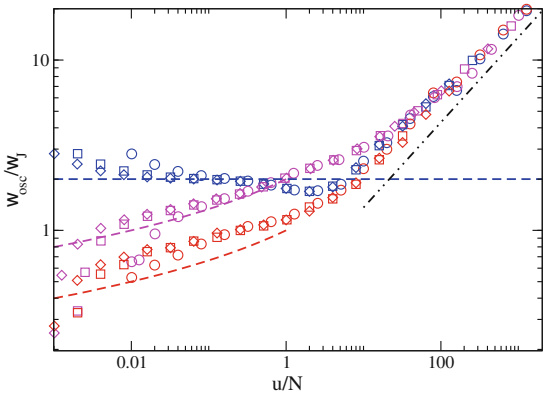

Fig. 7 The mean frequency of the $S_x(t)$ oscillations versus u/N for , and 1000(*diamond*) particles. The preparations are (*upper* to *lower* sets of data points): Zero (*blue*), Edge (*magenta*), and Pi (*red*). The weaker-interaction theoretical predictions (37–39), which are doubled due to mirror symmetry, are represented by *blue*, *red*, and *magentadashed lines*, while the strong interaction prediction (40) is represented by a *black dash-double-dotted line*

classical picture $\omega_{\rm osc}$ should be related to the Josephson frequency ω_J at the bottom of the sea, while quantum mechanically it reflects the level spacings of the participating levels. A straightforward analysis leads to the followings estimates:

$$\omega_{\rm osc} \approx 2\omega_J \quad [\text{Zero}] \tag{37}$$

$$\omega_{\rm osc} \approx 1\times\left[\log\left(\frac{N}{u}\right)\right]^{-1} 2\omega_J \quad [\text{Pi}] \tag{38}$$

$$\omega_{\rm osc} \approx 2\times\left[\log\left(\frac{N}{u}\right)\right]^{-1} 2\omega_J \quad [\text{Edge}] \tag{39}$$

$$\omega_{\rm osc} \approx \left(\frac{u}{N}\right)^{1/2} 2\omega_J \quad [u \gg N] \tag{40}$$

The first three expressions apply for $(u/N)<1$, where the differences between the preparations is distinct. The last expression refers to the regime $(u/N) > 1$ where the differences are blurred and the three preparations become equivalent equatorial states (as clearly evident from Fig. 7). Note that due to the mirror symmetry of the Zero preparation the expected frequency should approach $2\omega_J$, while for the Pi preparation it is bound from below by $2\omega_x$. Both frequencies are indicated in Fig. 7 by dashed lines.

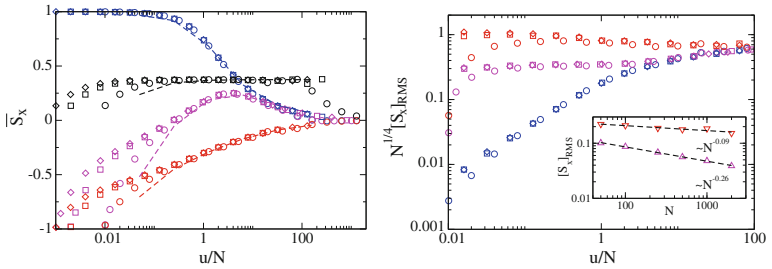

Fig. 8 *Left:* The long-time average of $S_x(t)$ versus u/N for , and 1000(*diamond*) particles. The preparations are (*upper* to *lower* sets of data points): Zero (*blue*), TwinFock (*black*), Edge (*magenta*), and Pi (*red*). The symbols are used for the quantum results and the *dashed lines* are the semiclassical prediction for 40 particles. Note that the scaling holds only in the Josephson regime $1 \ll u \ll N^2$, and therefore, for a given u/N range, becomes better for large N. *Right:* The long time RMS of $S_x(t)$ for the three coherent preparations (*lower* to *upper* sets): Zero (*blue*), Edge (*magenta*), and Pi (*red*). In the *inset*, the RMS of $S_x(t)$ for Edge (*triangle*) and Pi (*down-pointing triangle*) preparations is plotted versus N while $u = 4$ is fixed

5.3 Long Time Average

Next we examine the long time average, plotted in Fig. 8 as a function of the characteristic parameter. Unlike the fluctuations around it, this average value does not reflect the quantization of energy and therefore a purely semi-classical analysis is adequate. The naive expectation might be that coherence would be diminished due to phase spreading (aka "phase diffusion"). This is indeed the case in the Fock regime, leading to $\langle S_x \rangle_\infty \approx 0$. However, the situation is rather more complicated in the Josephson regime, where $\langle S_x \rangle_\infty$ is determined by u/N. The semi-classical phase space picture allows to calculate the phase distribution $P(\varphi)$ that pertains to the long time ergodic-like distribution (see for example Fig. 5). This distribution is determined by the LDOS. Then we use the integral

$$\overline{S_x} \approx \int \cos(\varphi) \mathrm{P}(\varphi) d\varphi, \tag{41}$$

to evaluate the residual coherence. This procedure results in the following predictions:

$$\overline{S_x} \approx 1/3 \quad [\text{TwinFock}] \tag{42}$$

$$\overline{S_x} \approx \exp[-(u/N)] \quad [\text{Zero}] \tag{43}$$

$$\overline{S_x} \approx -1 - 4/\log\left[\frac{1}{32}(u/N)\right] \quad [\text{Pi}] \tag{44}$$

Thus, the coherence of the Zero preparation is robustly maintained as long as $u/N < 1$, corresponding to the $\varphi = 0$ phase locking of the two condensates due to

the weak coupling. By contrast, the Pi and Edge coherence is far more fragile throughout the Josephson regime [32]. Note that the phase locking of the Pi state take place only in the Rabi-regime (no separatrix). As evident from the Twin-Fock self-induced coherence (46), one-particle coherence should not necessarily be lost due to interactions, but could actually be *built* [33]. This course of events is somewhat similar to the coherent relaxation of a system to its ground state at low temperatures: the ground state has higher purity compared with the initial preparation.

5.4 RMS of the Fluctuations

Finally, we turn to discuss the RMS of the fluctuations, which constitute a fingerprint of energy quantization. General reasoning implies that the *classical* fluctuations are suppressed by factor M:

$$\mathrm{RMS}\left[\langle A\rangle_t\right] = \left[\frac{1}{M}\int \tilde{C}_{\mathrm{cl}}(\omega)d\omega\right]^{1/2}. \tag{45}$$

In this formula $\tilde{C}cl(\omega)$ is the *classical* power spectrum of an ergodic trajectory. What we want to highlight is the *quantum* N dependence. It is important to clarify that in the *semi-classical* limit $M \to \infty$, and therefore the fluctuations are suppressed. We emphasize again that the quantum behavior is intermediate between the coherence-preserving *classical* (single trajectory) dynamics and the strong coherence-attenuation of the *semi-classical* (infinite M) dynamics.

The dependence of M on N is remarkably different for the various preparations. In the case of the TwinFock preparation $M \sim N$ and therefore the RMS is inversely proportional to $N^{1/2}$. This should be contrasted with the case of the Pi and the Edge preparations:

$$\mathrm{RMS}[S_x(t)] \sim N^{-1/2} \quad [\mathrm{TwinFock}] \tag{46}$$

$$\mathrm{RMS}[S_x(t)] \sim N^{-1/4} \quad [\mathrm{Edge}] \tag{47}$$

$$\mathrm{RMS}[S_x(t)] \sim (\log(N))^{-1/2} \quad [\mathrm{Pi}] \tag{48}$$

We further note that in the Pi case the leading dependence of the participation number is on the classical parameter ($M \sim u^{1/2}$), unlike the case of the Edge preparation where the leading dependence in on the quantum parameter ($M \sim N^{1/2}$). The results of the RMS analysis are presented in Fig. 8. The implied $N^{1/4}$ scaling based on Eq. (45) is confirmed. The dashed lines in the inset are power-law fits that nicely agree with the predictions of Eq. (46).

6 Summary

Using semiclassical machinery, we have analyzed the temporal fluctuation of the single-particle coherence, and of the fringe-visibility, in the Bose Josephson model. While recent experiments in the Josephson regime have essentially focused on mean-field population dynamics [8], with coherent preparations at the spectral extremes (self trapping versus Josephson oscillations), here we highlight intricate effects that can be found by studying the coherence-dynamics in the intermediate separatrix regime. We predict significant differences in the transverse relaxation of seemingly similar coherent initial states, differing by the initial relative-phase or by their location along the separatrix, as well as the interaction-induced phase-locking of two initially separated BECs due to the combined effect of interaction and coupling. The semiclassical WKB quantization facilitates the calculation of the LDOS for the pertinent preparations, and thus the estimation of the number of participating eigenstates. This allows for a detailed quantitative analysis of the time evolution of the fringe visibility function. The obtained analytic expressions are found to be in a very good agreement with the results of numerical calculations.

Acknowledgments The current manuscript summarizes the approach taken in a series of recent publications [32–35]. We acknowledge contributions to these works by Maya Chuchem, Erez Boukobza, Katrina Smith-Mannschott, Moritz Hiller, and Tsampikos Kottos. This research was supported by the Israel Science Foundation (grant nos. 29/11 and 346/11) and by Grant No. 2008141 from the United States-Israel Binational Science Foundation (BSF).

References

1. N. F. Ramsey, Phys. Rev. **78**, 695 (1950)
2. C. Bordé, Phys. Lett. A **140**, 10 (1989)
3. P.R. Berman, *Atom Interferometry* (Academic Press, San Diego, 1997)
4. D. Cronin, J. Schmiedmayer, D.E . Pritchard, Rev. Mod. Phys. **81**, 1051 (2009)
5. M.R. Andrews, C.G. Townsend, H.-J. Miesner, D.S. Durfee, D.M. Kurn, W. Ketterle, Science **275**, 637 (1997)
6. Y. Shin, M. Saba, T.A. Pasquini, W. Ketterle, D.E. Pritchard, A.E. Leanhardt, Phys. Rev. Lett. **92**, 050405 (2004)
7. Y.-J. Wang, D.J. Anderson, V.M. Bright, E.A. Cornell, Q. Diot, T. Kishimoto, M. Prentiss, R.A. Saravanan, S.R. Segal, S. Wu, Phys. Rev. Lett. **94**, 090405 (2005)
8. M. Albiez, R. Gati, J. Folling, S. Hunsmann, M. Cristiani, M.K. Oberthaler, Phys. Rev. Lett. **95**, 010402 (2005)
9. G.-B. Jo, Y. Shin, S. Will, T.A. Pasquini, M. Saba, W. Ketterle, D.E. Pritchard, M. Vengalattore, M. Prentiss, Phys. Rev. Lett. **98**, 030407 (2007)
10. G.-B. Jo, J.-H. Choi, C.A. Christensen, T.A. Pasquini, Y.-R. Lee, W. Ketterle, D.E. Pritchard, Phys. Rev. Lett. **98**, 180401 (2007)
11. G.-B. Jo, J.-H. Choi, C.A. Christensen, Y.-R. Lee, T.A. Pasquini, W. Ketterle, D.E. Pritchard, Phys. Rev. Lett. **99**, 240406 (2007)
12. T. Schumm, S. Hofferberth, L.M. Andersson, S. Wildermuth, S. Groth, I. Bar-Joseph, J. Schmiedmayer, P. Krüger, Nat. Phys. **1**, 57 (2005)

13. S. Hofferberth, I. Lesanovsky, B. Fischer, T. Schumm, J. Schmiedmayer, Nature (London) **449**, 324 (2007)
14. J. Esteve, C. Gross, A. Weller, S. Giovanazzi, M.K. Oberthaler, Nature **455**, 1216 (2008)
15. P. Böhi, M.F. Riedel, J. Hoffrogge, J. Reichel, T.W. Hänsch, P. Treutlein, Nat. Phys. **5**, 592 (2009)
16. C. Gross, T. Zibold, E. Nicklas, J. Esteve, M.K. Oberthaler, Nature **464**, 1165 (2010)
17. M.F. Riedel, P. Böhi, Y. Li, T.W. Hänsch, A. Sinatra, P. Treutlein, Nature **464**, 1170 (2010)
18. Z. Chen, J.G. Bohnet, S.R. Sankar, J. Dai, J.K. Thompson, Phys. Rev. Lett. **106**, 133601 (2011)
19. B. Lüke, M. Scherer, J. Kruse, L. Pezze, F. Deuretzbacher, P. Hyllus, O. Topic, J. Peise, W. Ertmer, J. Arlt, L. Santos, A. Smerzi, C. Klempt, Science **334**, 773 (2011)
20. R. Bücker et al., Nat. Phys. **7**, 608 (2011)
21. J. Javanainen, M. Wilkens, Phys. Rev. Lett. **78**, 4675 (1997)
22. J. Javanainen, M. Wilkens, Phys. Rev. Lett. Phys. Rev. Lett. **81**, 1345 (1998)
23. A. Vardi , J.R. Anglin, Phys. Rev. Lett. **86**, 568 (2001)
24. J.R. Anglin, A. Vardi, Phys. Rev. A **64**, 013605 (2001)
25. M. Greiner, O. Mandel, T.W. Hänsch, I. Bloch, Nature **419**, 51 (2002)
26. A. Widera, S. Trotzky, P. Cheinet, S. Fölling, F. Gerbier, I. Bloch, V. Gritsev, M.D. Lukin, E. Demler, Phys. Rev. Lett. **100**, 140401 (2008)
27. J. Grond, U. Hohenester, I. Mazets, J. Schmiedmayer, New J. Phys. **12**, 065036 (2010)
28. I. Tikhonenkov, M.G. Moore, A. Vardi, Phys. Rev. A **82**, 043624 (2010)
29. J. Grond, U. Hohenester, J. Schmiedmayer, A. Smerzi, Phys. Rev. A **84**, 023619 (2011)
30. E.M. Wright, D.F. Walls, J.C. Garrison, Phys. Rev. Lett. **77**, 2158 (1996)
31. S. Will, T. Best, U. Schneider, L. Hackermüller, D.S. Lühmann, I. Bloch, Nature **465**, 197 (2010)
32. E. Boukobza, M. Chuchem, D. Cohen, A. Vardi, Phys. Rev. Lett. **102**, 180403 (2009)
33. E. Boukobza, D. Cohen, A. Vardi, Phys. Rev. A **80**, 053619 (2009)
34. K. Smith-Mannschott, M. Chuchem, M. Hiller, T. Kottos, D. Cohen, Phys. Rev. Lett. **102**, 230401 (2009)
35. M. Chuchem, K. Smith-Mannschott, M. Hiller, T. Kottos, A.Vardi, D. Cohen, Phys. Rev. A **82**, 053617. Optionally arXiv:1001.2120, which includes extra appendices
36. Y. Li, P. Treutlein, J. Reichel, A. Sinatra, Eur. Phys. J. B **68**, 365 (2009)
37. M. Kitagawa, M. Ueda, Phys. Rev. A **47**, 5138 (1993)
38. M.J. Holland, K. Burnett, Phys. Rev. Lett. **71**, 1355 (1993)
39. L. Pezze, A. Smerzi, Phys. Rev. Lett. **102**, 100401 (2009)
40. K.W. Mahmud, H. Perry, W.P. Reinhardt, Phys. Rev. (A) **71**, 023615 (2005)
41. R. Gati, M.K. Oberthaler, J. Phys. B **40**, R(61) (2007)
42. Franzosi et al., Int. J. Mod. Phys. B (14), 943 (2000)
43. E.M. Graefe, H.J. Korsch, Phys. Rev. A **76**, 032116 (2007)
44. D. Witthaut, E.M. Graefe, H.J. Korsch, Phys. Rev. A **73**, 063609 (2006)
45. E.M. Graefe, H.J. Korsch, A. E. Niederle, Phys. Rev. A **82**, 063628 (2010)
46. F. Nissen, J. Keeling, Phys. Rev. A **81**, 063628 (2010)
47. J.C. Varilly, J.M. Gracia-Bondia, Ann. Phys. **190**, 107 (1989)
48. C. Brif, A. Mann, J. Phys. A **31**, L(9) (1998)
49. G.S. Agarwal, Phys. Rev. A. **24**, 2889 (1981)
50. J.P. Dowling, G.S. Agarwal, W.P. Schleich, Phys. Rev. A **49**, 4101 (1994)
51. S. Giovanazzi, A. Smerzi, S. Fantoni, Phys. Rev. Lett. **84**, 4521 (2000)
52. F.S. Cataliotti, S. Burger, C. Fort, P. Maddaloni, F. Minardi, A. Trombettoni, A. Smerzi, M. Inguscio, Science **293**, 843 (2001)
53. S. Levy, E. Lahoud, I. Shomroni, J. Steinhauer, Nature **449**, 579 (2007)
54. C. A Sackett, Nature **449**, 546 (2007)
55. A. Smerzi, S. Fantoni, S. Giovanazzi, R.S. Shenoy, Phys. Rev. Lett. **79**, 4950 (1997)